Available online at www.sciencedirect.com

jmr&t Journal of Materials Research and Technology

journal homepage: www.elsevier.com/locate/jmrt

Original Article

# Correlations between processing technology, microstructure and properties of a Ni-rich Ti–Ni shape memory alloy

*Eduardo M. Sashihara* [a,*], *Pedro N. Inoue* [b], *Odair D. Rigo* [c], *Nelson B. Lima* [a], *Jorge Otubo* [a,b]

[a] *Materials Science and Technology Center, Instituto de Pesquisas Energéticas e Nucleares (IPEN)/USP, São Paulo, SP, Brazil*

[b] *Department of Materials and Processes, Instituto Tecnológico de Aeronáutica (ITA), São José Dos Campos, SP, Brazil*

[c] *Materials Laboratory, Centro Tecnológico da Marinha (CTM), São Paulo, SP, Brazil*

ARTICLE INFO

*Article history:*
Received 31 May 2022
Accepted 17 August 2022
Available online 24 August 2022

*Keywords:*
Ni–Ti Forming
Microstructure and properties
Martensitic transformation

ABSTRACT

A Ti-50.8Ni (at.%)/Ti-55.9Ni (wt.%) VIM processed ingot was rotary swaged and rolled in parallel, obtaining bars with a total Area Reduction above 90% (from forged/rolled raw state one). Throughout the successive stages, the microstructural evolution, thermal and mechanical properties were compared. Deformation bands, grain morphology, precipitates and oxidation were evaluated (by OM and SEM/EDS). An essentially (~100%) austenitic phase was detected at room temperature (via XRD/Rietveld method), while the Martensitic Transformation temperatures occurred at negative temperatures (via DSC). The rolled bar got through the process more regularly, with homogeneous and refined structure. Typical defects such as superficial microcracks and creases were relevant in the last stages of the two-dies rotary swaging with inductive heating. The work hardening level (via Hardness Test) was similar in both metal forming processes, being 5–7% more pronounced at the edge area of the bars due to redundant work.



## 1. Introduction

The Ni–Ti (or Ti–Ni) alloys with Shape Memory Effect/Superelasticity (SME/SE) have numerous and resourceful applications, offering design flexibility and enhanced performance areas across multiple use cases. This occurs owing to its intrinsic and outstanding shape recovery (~8%), vibration/noise damping capacity, etc. Besides having excellent mechanical properties, they are fatigue, wear and corrosion resistant, and highly biocompatible.

The feature of SME/SE is largely related to the crystallographic reversibility of Martensitic Transformation (MT), either mechanically or thermally assisted. The properties of the Ni–Ti alloys are mainly dependent on composition, microstructure and thermomechanical processing, whereby the temperature for

* Corresponding author.
E-mail address: sashihara@usp.br (E.M. Sashihara).

https://doi.org/10.1016/j.jmrt.2022.08.087

shape recovery can vary from −50 to 110 °C [1,2]. However, the production and processing of these alloys are relatively expensive, time-consuming and laborious, requiring high-purity materials and well-controlled processes across multiple stages [3]. As a result, it is considered to be of strategic value by the different sovereigns with the technical capability to adapt this alloy to the growing global market demand (*tailor-made*). We have been producing Ni–Ti alloy ingots weighing around 20 kg by VIM and EBM [4,5]. More recently, research related to thermomechanical processing has outlined processes to produce more basic alloy forms, such as bars and wires [6–8]. Despite this, a systematic study correlating thermomechanical processing to alloy microstructure and properties has not yet been published and the literature on this subject is scarce. In fact, as predicting the results and evolution of microstructural characteristics from secondary processes (such as work hardening, present phases and their transformations, homogeneity of deformation, precipitation, defects), it is possible to develop products with adequate properties for potential applications. In nickel-rich Ti–Ni alloys, precipitates can be used to adjust the MT temperatures [1,4].

In this paper, a demanding Ti–Ni alloy has been accordingly processed by rotary swaging and rolling. Both mentioned metals forming processes consist of plastically deforming the material (in radial and axial directions) by direct compression, usually under hot condition (above the recrystallization temperature). Rotary swaging is a continual radial hammering of a bar; while rolling is a process in which a bar is forced through a gap between cylinders/rollers in opposite rotation [3,9,10]. Bar samples of successive steps were characterized and compared in terms of microstructural evolution, mechanical and thermal properties, which are related to SME/SE.

## 2. Materials and methods

The Ni-rich Ti–Ni alloy consisted of a 20 kg ingot, 90 mm in diameter, produced by Vacuum Induction Melting (VIM). The nominal composition was Ti-50.8Ni (at.%) / Ti-55.9Ni (wt.%) with carbon (0.022 wt.%) and oxygen (0.047 wt.%) contents, confirmed by XRF/ICP analyzes. The as-cast ingot was hot forged in a hydraulic press down to 50 mm in diameter, and then hot rolled down to 16 mm in diameter bar, the starting material for this work.

As summarized in Fig. 1, the ~16.0 mm in diameter bar (P0) was solution treated (800 °C/ 60 min) and then hot-rotary swaged in a FENN 4 Dies swager down to ø ~ 12.0 mm ($L_f$ = 735.0 mm long) in 3 passes (PF1, PF2 and PF3), totaling an Area Reduction (AR) of 43.9%. Thus, this pre-formed bar (PF3, ø ~ 12.0 mm) was divided into two halves ($L_{f/2}$ = 367.5 mm long) and one part continued with hot rotary swaging down to ø ~ 4.5 mm (S1–S10: $AR_{total}$ = 92.1%). Bellow 9.525 mm swaging die, the bar was swaged in a FENN 2 Dies swager. Another half was rolled in a FENN 5HP duo-channels rolling mill down to ø ~ 3.5 mm (R1–R8: $AR_{total}$ = 95.2%).

Before the thermomechanical processing steps, the bar was visually inspected and some surface defects due to rolling/swaging steps were removed by mechanical grinding. The interpass heating during Hot-Rotary Swaging (H-S) or Hot-Rolling (H-R) was done at ~800 °C with 15 min soaking time. As planned, for Samples S8 thru S10, the bar experimented a continuous electromagnetic inductive heating during its H–S and; for Sample R8, the bar was annealed at ~750 °C/ 10 min, slowly cooled, and then Cold-Rolled (C-R) at room temperature (RT).

Regarding the metallography, all the bar samples were grinded (SiC sandpapers: #180 down to #2000 grit), mechanically polished (diamond paste: 6 to 1 μm) and etched in a solution (90 ml $H_2O$ + 10 ml $HNO_3$ + 1 ml HF). The initial observation was done by Optical Microscopy (OM) using the Olympus BX51M microscope with Image-J software. Other details (including chemical mapping into samples without etching) were analyzed by Scanning Electron Microscopy with Energy Dispersion Spectroscopy (SEM/EDS), under the JEOL JSM-6701 F microscope (working voltage: 2.0–6.0 kV via

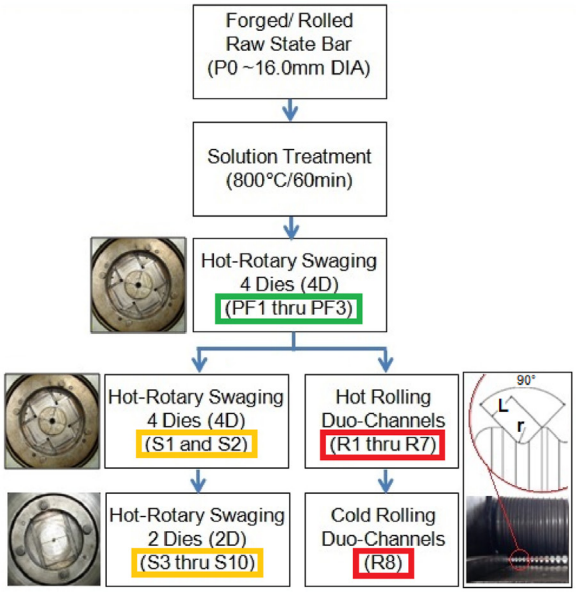


| Samples ID | Channel (mm) | | Ø Bar (mm) | AR (%) |
|---|---|---|---|---|
| Start: P0 | Dies | Ø (mm) | ~16.0 | - |
| PF1 | 4D | 16.002 | 15.80 | 2.5 |
| PF2 | | 13.843 | 13.64 | 25.5 |
| PF3 | | 11.938 | 11.98 | 22.8 |
| | - | | ~12.0 | Partial: **43.9** |
| S1 | 4D | 10.414 | 10.88 to 10.42 | 24.3 |
| S2 | | 9.525 | 9.71 to 9.44 | 17.9 |
| S3 | 2D | 8.763 | 9.36 to 9.24 | 4.2 |
| S4 | | 7.620 | 8.60 to 8.32 | 18.9 |
| S5 | | 6.350 | 7.51 to 7.44 | 20.0 |
| S6 | | 6.350 | 7.35 to 7.14 | 7.9 |
| S7 | | 4.953 | 6.22 to 6.12 | 26.5 |
| S8 | | 4.267 | 5.84 to 5.23 | 27.0 |
| S9 | | 3.683 | 5.02 | 7.9 |
| End: S10 | | 3.175 | 4.50 to 4.37 | 24.2 |
| | - | | ~4.5 | Total: **92.1** |
| - | r (mm) | L (mm) | - | - |
| R1 | 3.1 | 9.4 | 10.14 | 28.3 |
| R2 | 2.7 | 8.0 | 8.85 to 8.67 | 26.9 |
| R3 | 2.1 | 6.3 | 7.20 to 7.15 | 32.0 |
| R4 | 1.6 | 4.9 | 5.63 to 5.56 | 39.5 |
| R5 | 1.5 | 4.5 | 5.25 to 5.23 | 11.5 |
| R6 | 1.4 | 4.2 | 4.53 to 4.46 | 27.3 |
| R7 | 1.2 | 3.6 | 4.26 to 3.88 | 24.3 |
| End: R8 | 1.0 | 3.0 | 3.60 to 3.48 | 11.5 |
| | - | | ~3.5 | Total: **95.2** |

**Fig. 1 – Diagram of a secondary metal forming of the bar, from ø ~ 16 mm down to 4.5 and 3.5 mm.**

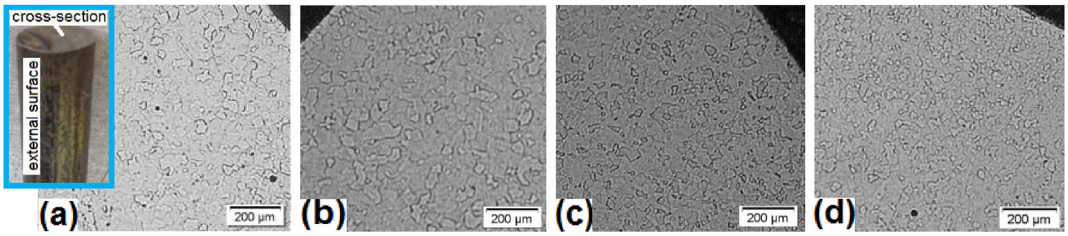


**Fig. 2 – OM-images of raw-state bar (a) P0; pre-formed bar: (b) PF1, (c) PF2, (d) PF3.**

secondary electrons, or 12.0–15.0 kV via backscattered electrons).

The main phases were also identified/quantified at RT by X-ray diffraction (XRD) with Rietveld method into the starting ø ~ 16.0 mm (P0) and endings ø ~ 4.5 mm (S10) / ~3.5 mm (R8), at cross-section etched, using the Rigaku MULTIFLEX Diffractometer with the following: program (GSAS), monochromator (graphite), radiation (Cu-K$\alpha$, 40 kV, 20 mA), scanning (2$\theta$: 10°–90°, step: 0.025°, t: 15 s/step).

The mechanical properties of the bars were analyzed by hardness distribution maps along the cross-section obtained by ~60 thru ~180 indentations (min. distance each other ~0.5 mm), in an automated EMCOTEST DuraScan-50 durometer, by Vickers method 0.5HV, objective lens 40×, magnification level 1 (load 500 gf, time ~5 s).

The direct and reverse Martensitic Transformation (MT) temperatures and enthalpy changes were determined via Differential Scanning Calorimetry (DSC) according to ASTM F2004-05(2010) using a DSC-404C from NETZSCH. The furnace chamber was evacuated and purged with argon gas twice, and then, the DSC thermal cycle was done in a protective helium gas at 5 °C/ min rate. This thermal cycle consisted of: (a) initial heating from 20 to 120 °C; (b) a first plateau of strain relief at 120 °C/ 10 min; (c) a cooling from 120 to −80 °C; (d) a second plateau of thermal stability at −80 °C/ 10 min; (e) a new heating from −80 to 120 °C, to determine the temperatures of the reverse MT; (f) a third plateau (=item b); (g) a new cooling from 120 to −80 °C, to determine the temperatures of the direct MT; (h) a last plateau and heating just to return to RT.

## 3. Results and discussion

In terms of processes in Fig. 1, some minor inaccuracies are noticeable: (a) in general, bar dimensions (ø) are larger than tool channel ones (ø or L), whose difference (after each step) is difficult to predict or regulate in light of the thermal, elastic/SE shape recovery of material and adjustment to tool gap (as mismatched shims, incomplete closing of dies); (b) in rolling, the tool channel has rounded corners with a radius (r) that is proportional to the side (L), and the rolled bar is not completely circular (the value of ø is an approximate one); (c) the bar cools (since it leaves the furnace) and heats (due to friction and redundant work) unequally during the hot-working; (d) bar feeding speed and temperature threshold are not settled.

In spite of the process controls (as real temperature and heating time) are difficult, as they depend on bar variables and its manual feeding, all the hot-working stages have been completed above the material's recrystallization temperature (around 550 °C) [1,3,11], upon which the semi-quantitative correlations are based.

In Fig. 2(a), further its preliminary thermomechanical processing, the forged/rolled raw-state bar, Sample P0 (ø ~ 16 mm), presented a granular structure at cross-section, with a relatively smooth external surface [in detail], for this subsequent work. In Fig. 2(b–d), the pre-formed bar had a similar microstructure, until the third Sample PF3 (ø ~ 12 mm) still showing evenly-distributed and near-equiaxed grains, as in [11].

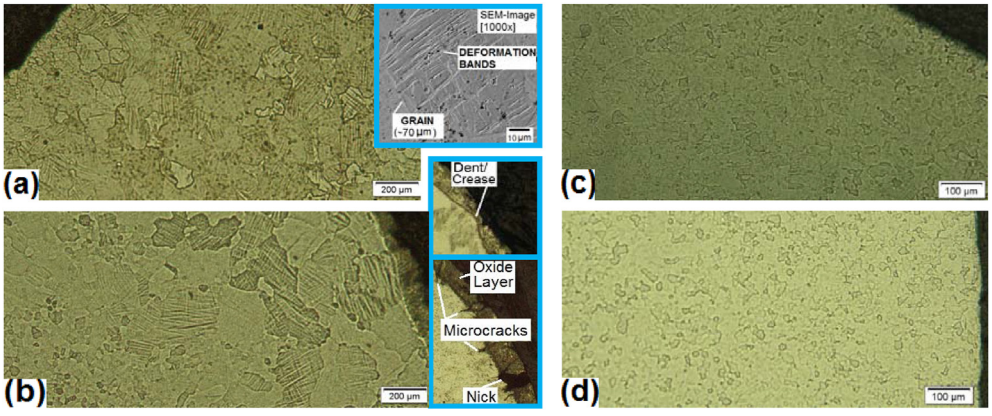


**Fig. 3 – OM-images of swaged & rolled bars, samples: (a) S1; (b) S8; (c) R1; (d) R8 [In details]: Typical deformation bands (as in S1) & surface defects (as in S8), for reference.**

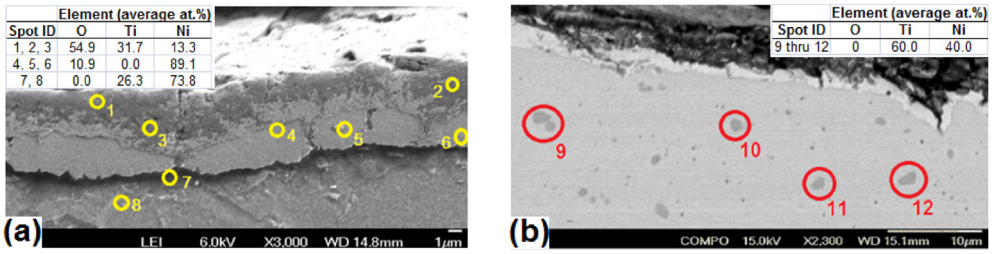


**Fig. 4 – SEM-images of swaged bar, sample S5: (a) At longitudinal section, with etching; (b) at cross-section, without etching.**

Fig. 3 corresponds to the OM-images of the swaged and rolled bars cross-section, as in Samples S1, S8, R1 and R8 (taken after each metal forming step) for reference.

According to Fig. 3(a), Sample S1 (ø ~ 10.6 mm) presented many deformation bands [as is in detail] visible within several rough grains (average grain size ~120 μm) along its entire cross-section, after the Area Reduction (AR) of 24.3%. Following the swaging process, the microstructure remained homogeneous, generally more fine-grained (recrystallized) with deformation bands. Notwithstanding, in the later three stages, its structure reached heterogeneity, with near-equiaxed grains (~40 μm) in the center region only and deformation bands in irregularly larger grains (~90–180 μm) from the middle-radius to surface, in addition to an oxide layer which increased from <10 μm to ~90 μm thick, as in Sample S8 (ø ~ 5.5 mm), see Fig. 3(b) in detail. Outside of an AR of 27.0%, it is likely that this resulting heterogeneity is due in part to the rapid inductive heating (not uniform in all cross-section) experienced in Samples S8 thru S10; being thinner it heats up and cools more quickly leaving insufficient time for a complete recrystallization, and/or with an abnormal growth of peripheral grains (harder, as discussed hereafter). Still [in detail, Fig. 3(b)], some typical surface defects as microcracks (~100 μm max deep), nick and dent/crease were mainly found on the last 2D-swaged bar samples. Microcracks seem as irregular line (transverse or longitudinal) scratches of any depth. Nick resembles a small gouge with sharp edges. Dent/crease is a just depressed or folded back part upon itself in such a manner that its boundaries are smooth or in channels like long upsetting. These defects are mostly caused by the impact of two-dies during the swaging with relatively larger opening toward the bar. Anyway, after grinding them, the clean bar has a negligible cross-sectional change (just smooth/local blend-out).

In parallel, Fig. 3(c), Sample R1 (ø ~ 10.1 mm) also presented deformation bands (although they are not so evident in this magnification) within fine-grained (~25–75 μm) along the cross-section, as a consequence of the AR of 28.3%. In hot rolling sequence, the samples continued homogeneously refined and with typical deformation bands. At the end, Fig. 3(d), there was a still homogeneous structure, delineated contours of near-equiaxed and well-recrystallized grains (~20–30 μm), with no deformation bands, relative to AR of 11.5% at RT for Sample R8 (ø ~ 3.5 mm).

More particularly, Fig. 4 illustrates a cumulative surface oxide layer (as in Sample S5), and existing precipitates within the matrix, as a result of the hot working. In this stage via SEM, it was already feasible to notice the formation of microcracks crossing the oxide layer toward the matrix.

From the SEM/EDS analysis, it is possible to outline some characteristics, such as chemical heterogeneity in this oxide layer down to the matrix level. In Fig. 4(a), this layer appears to be visually composed of two (or more) sublayers on the Sample S5, for instance: a darker surface, at spots 1 thru 3 with [1.3Ni:3.2Ti:5.5O] ratio; and another layer underneath, at spots 4 thru 6 with [8.9Ni:0Ti:1.1O] ratio. In the adjacent matrix, at

**Table 1 – Vickers hardness values of bar samples.**

| Samples ID | Bar ~Ø (mm) | Area reduction AR (%) | Average Hardness near Center (HV) | Average Hardness near ½Radius (HV) | Average Hardness near Edge (HV) | Quantity of Indentation (each) | Standard Deviation (HV) |
|---|---|---|---|---|---|---|---|
| P0 | 16.0 | – | 252.5 | 258.6 | 271.7 | 180 | 12.1 |
| PF1 | 15.8 | 2.5 | 238.4 | 253.8 | 258.2 | 161 | 11.2 |
| PF2 | 13.6 | 25.5 | 229.2 | 236.0 | 244.4 | 123 | 11.3 |
| PF3 | 12.0 | 22.8 | 238.5 | 244.0 | 248.6 | 92 | 11.6 |
| S1 | 10.6 | 24.3 | 308.1 | 304.0 | 310.7 | 65 | 13.0 |
| S4 | 8.5 | 18.9 | 250.3 | 249.0 | 253.0 | 128 | 8.8 |
| S5 | 7.5 | 20.0 | 252.0 | 261.8 | 278.3 | 150 | 15.3 |
| S8 | 5.5 | 27.0 | 283.2 | 289.9 | 314.7 | 132 | 23.0 |
| S10 | 4.5 | 24.2 | 330.8 | 347.3 | 352.7 | 154 | 13.7 |
| R1 | 10.1 | 28.3 | 246.2 | 247.8 | 262.3 | 82 | 18.5 |
| R2 | 8.8 | 26.9 | 260.9 | 271.6 | 288.5 | 119 | 19.1 |
| R3 | 7.2 | 32.0 | 291.9 | 297.6 | 305.6 | 61 | 13.9 |
| R4 | 5.6 | 39.5 | 295.5 | 305.8 | 317.6 | 102 | 25.5 |
| R8 | 3.5 | 11.5 | 260.4 | 260.1 | 268.4 | 82 | 8.9 |

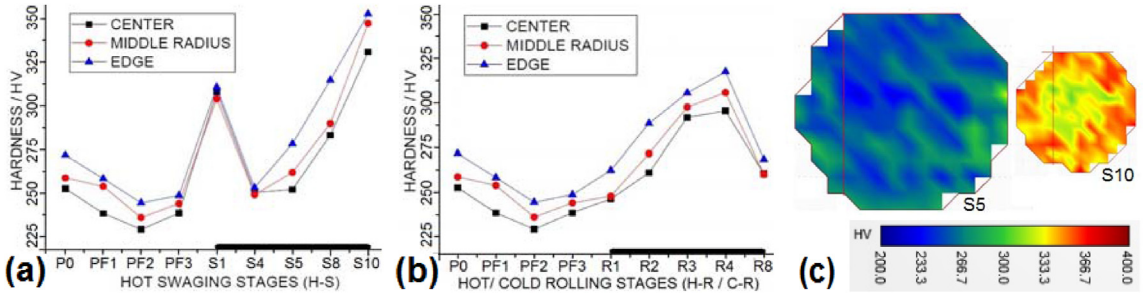


**Fig. 5 – Hardness trend analysis: (a) H-S and (b) H-R/C-R stages. (c) Hardness distribution maps of samples S5 and S10, for reference.**

spots 7 and 8 [7.4Ni:2.6Ti] ratio, without O. According to the literature [12–14], these particular results could occur due to the high reactivity of Ti to O (with low solubility limit), involving preferential diffusion of these elements in opposite directions, with subsequent formation of oxides and precipitates, which caused changes in chemical composition in the region. Fig. 4(b) shows the Sample S5 just polished, such that, $Ti_2Ni$ precipitates were identified, as larger (~1.5 μm), rounded and dark gray ones, sparsely inside the matrix (TiNi), by EDS analysis at spots 9 thru 12, with ~60 at.% of Ti and ~40 at.% of Ni. As a result, the similar $Ti_4Ni_2O$ would also be possible, as the O content is over its solubility limit (150 $ppm_{,wt}$), whereas the squared TiC seems improbable, as the C content is close to its solubility limit (250 $ppm_{,wt}$). The formation of these precipitates enriches the surrounding matrix with Ni, which can significantly decrease the MT temperatures [4,15,17].

Table 1 refers to hardness measurements on the bar samples cross-section after each H-S and H-R/C-R step, highlighting those previously chosen, scattered and/or sequential samples.

In Fig. 5(a and b), more accurately per bar stage, the average hardness values have increased in the radial direction indeed, from the center to the edge area (from 4th to 6th columns in Table 1), in +5.6% by H-S and +6.5% by H-R/C-R. It is readily evidenced in terms of hardness distribution maps. In Fig. 5(c), for one, its color gradient is mostly bluish (softer) in Sample S5 near the center, and reddish (harder) in Sample S10 near the edge (with deformation bands into rough grains, as similarly shown in Fig. 3(b) for Sample S8). In swaging, the effect of radial compression is more superficial, where a certain tangential shear component generates an incremental redundant work, becoming harder and less smooth [7,16].

Concerning the hardness trends, Sample P0 (at forged/rolled raw state) started slightly harder due to the bar preliminary processing. After a solution heat treatment, the bar followed the first 4D-swaging step with AR of 2.5% just to straighten it, then Sample PF1 continued practically in its previous solution treated state (less hard). Secondly, Sample PF2 hardness decrease could be attributed to a mechanical-thermal energy transfer balance point, when the deformed material volume is large, its redundant work per AR increases as well, raising the real temperature which brings out additional dynamic recrystallization (softer bar). Thirdly, Sample PF3 became slightly harder, when the work hardening level starts to prevail against it.

Following the H-S in Fig. 5(a), excepting Sample S1 with hardness ≥300HV (it is unclear – if occurred an unexpected delay/cooling in the H-S), Samples S4 thru S10 presented a hardness increase, that is, a cumulative work hardening not eliminated by pre-heating the bar, being more expressive for later stages, Samples S8 thru S10, where the hardness upward shift was supposedly boosted by rapid, experimental inductive heating (the smaller diameter, as it cools first, the harder the bar is).

Comparatively in Fig. 5(b), from the initial H-R sequence of the bar (Samples R1 thru R4), the hardness seems to be increasing with the progression of AR (from 28.3 to 39.5%). For the last step (Sample R8), annealed previously and then C-R, the hardness reduced after a smaller AR of 11.5% at RT, that is, still close to its overall average hardness. Beyond this, the rolled bar (Ø ~ 3.5 mm × 1780.0 mm long) showed a more homogeneously fine-grained structure, Fig. 3(d), and better surface finish.

All hardness values are indirectly related to amounts of AR of each inherent sample stage (in Table 1), as indicative ones

**Table 2 – Temperatures and enthalpy changes of martensitic transformation of bar samples.**

| Samples ID | Bar ø (mm) | $M_s$ (°C) | $M_p$ (°C) | $M_f$ (°C) | $H_M$ (J/g) | $A_s$ (°C) | $A_p$ (°C) | $A_f$ (°C) | $H_A$ (J/g) | $A_p$-$M_p$ (°C) |
|---|---|---|---|---|---|---|---|---|---|---|
| P0[a] | ~16.0 | −36.7 | −44.2 | −53.4 | −8.3 | −21.6 | −15.5 | −11.8 | 13.3 | 28.7 |
| PF1 | ~15.8 | −32.4 | −37.6 | −45.3 | −10.9 | −17.6 | −13.0 | −11.1 | 15.2 | 24.6 |
| PF2 | ~13.6 | −30.8 | −36.9 | −43.3 | −10.9 | −16.7 | −11.1 | −8.7 | 13.6 | 25.8 |
| PF3 | ~12.0 | −29.6 | −34.4 | −41.2 | −11.0 | −16.0 | −11.2 | −8.8 | 12.9 | 23.2 |
| S10 | ~4.5 | −40.0 | −43.0 | −47.7 | −12.5 | −17.2 | −12.6 | −9.9 | 14.9 | 30.4 |
| R8 | ~3.5 | −37.9 | −41.2 | −45.5 | −13.3 | −17.1 | −12.5 | −9.7 | 16.8 | 28.7 |

[a] First DSC data are indicated in Fig. 6(a), as reference.

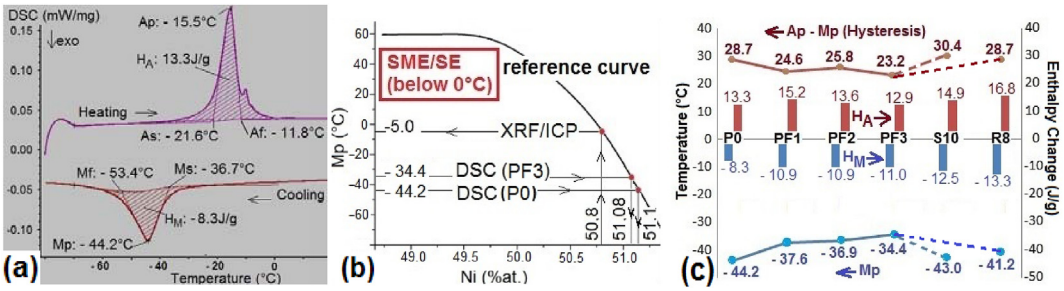


**Fig. 6 – (a) Original DSC Curve for Sample P0; (b) Reference Curve: $M_p$ × Ni Relation [4]; (c) $A_p$–$M_p$ (Hysteresis), $M_p$ Temperature, $H_A$ and $H_M$ Enthalpy Changes Trend Analysis.**

(not easily linked) because of other minor process inaccuracies, as bar feeding speed and real temperature (as stated previously). In general, swaged and rolled bars had an approximate parallelism of hardness which indicates a balance of mechanical properties between them, with a cumulative work hardening of material, even though the interpass heating relieves part of that [3,11]. Regardless of the processing techniques, Table 1 and Fig. 5 show clearly the radial hardness increase for each stage which is attributed to redundant work. Similar results of radial hardness increase were presented by Antunes [7] on cold wire drawing and by Shahmir et al. [16] using high-pressure torsion on Ni–Ti alloys.

Table 2 summarizes some DSC data from bar samples and Fig. 6(a) exemplifies an original DSC curve (for Sample P0) with $M_s$, $M_p$, $M_f$ & $A_s$, $A_p$, $A_f$ (*start, peak, finish*) temperatures of direct & reverse Martensitic Transformation and respective $H_M$ & $H_A$ enthalpy changes (area under each associated curve). Fig. 6(b) refers to a named Reference Curve: $M_p$ × Ni Relation [4]; and Fig. 6(c) relates $A_p$-$M_p$ hysteresis to $M_p$ temperature, including the $H_M$ and $H_A$ enthalpy changes trend analysis.

According to Otubo et al. [4], there is a direct relationship between the $M_p$ temperature and the matrix nickel content, as per a reference curve, Fig. 6(b). Therefore, when relating this curve to the maximum and minimum values of $M_p$, −34.4 °C and −44.2 °C (measured via DSC), between the raw-state bar (ø ~ 16.0 mm) down to swaged and rolled bars (ø ~ 4.5 and ~3.5 mm), a negligible deviation of chemical homogeneity in the material is pointed out, whose composition would be between 51.08 and 51.1 Ni (at.%). In turn, given the nominal composition of 50.8 Ni (at.%), the $M_p$ temperature would be −5.0 °C by using the reference curve, that is, substantiating this significant difference in $M_p$ on the Ni-rich side of Ti–Ni alloys.

In Fig. 6(c), the enthalpy changes (*H*) presented close to each other, with $H_M$ varying from −8.3 to −13.3 J/g and $H_A$ from 13.3 to 16.8 J/g, between Samples P0 and R8. $H_M$ is minimum when $M_p$ is minimum (in Sample P0), $H_A$ is minimum when $M_p$ is maximum (in Sample PF3) and, as a whole, it seems that they tend to increase with the thermomechanical processing. Physically, the bar samples release less energy on cooling than they absorb it on heating ($H_M < H_A$) associated with the different relaxation of elastic energy during the direct and reverse MT [2], whose *H* values are within or lower than the expected ones for equiatomic composition and high purity Ti–Ni alloys, as a function of thermodynamic stability [15] and/or magnetic effect [17].

Regardless of the Samples P0 and R8 presented the same $A_p$–$M_p$ hysteresis (28.7 °C), its fluctuation along all samples could also be due to minor process inaccuracies. Inversely related to $M_p$ temperature trend, $A_p$–$M_p$ hysteresis varied between a minimum of 23.2 °C (for Sample PF3) and a maximum of 30.4 °C (for Sample S10), which are typical driving forces for thermoelastic MT of Ni–Ti alloys with SME/SE, as foreseen by Otubo et al. [15] and by Frenzel et al. [17].

At the end, Samples S10 and R8 are totally martensitic below −47.7 °C and −45.5 °C ($M_f$) and austenitic above −9.9 °C and −9.7 °C ($A_f$), respectively, thus both bars seem well aligned. Between $M_s$ and $M_f$ or $A_s$ and $A_f$ (which are approximate as they depend on the intersection method) the two phases coexist, reflecting narrow DSC curves (~7.5 °C wide). Moreover, it is worth emphasizing a relatively small variation of $M_p$ (1.8 °C) and $A_p$ (0.1 °C), the critical transition temperatures, between final bars with no subjectivity from evaluation,

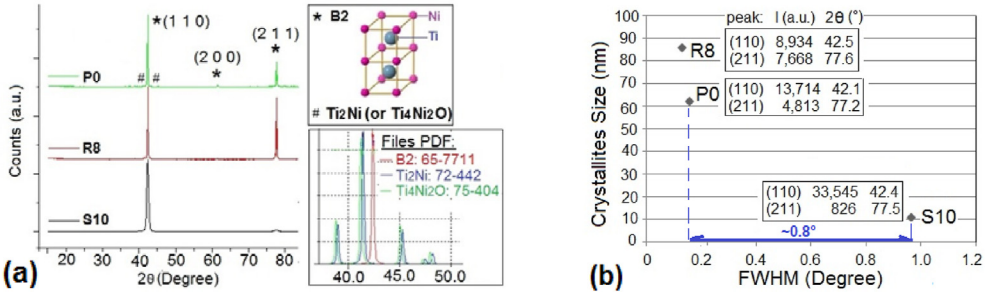


**Fig. 7 – (a) X-ray Diffractogram of Bar Samples: Raw-State P0, Swaged S10 and Rolled R8; (b) Crystallites Sizes of them with XRD Spectrum Data [in Detail] used in the Scherrer Equation.**

as a close thermomechanical processing correlation. In this context, they are definitely important for applications. For example, a commercial jet aircraft at a cruise altitude of 35,000 feet experiences an outside air temperature of −50 °C (below $M_f$), hence each flap (aerodynamic surface at wing trailing edge) with innovative actuator hypothetically made out of Ti–Ni bar can stay in the martensitic state (flaps retracted), and when it is heated to −5 °C (above $A_f$), while the aircraft is in the approach phase (landing), the Ti–Ni bar can naturally return to the austenitic state (extended flaps), that is, keeping the aircraft lift/drag ratio appropriately, given a cyclic recovery of the original form by SME. In addition, the flaps can deform continuously at a low stress level or more easily at low temperatures.

The starting and final Samples (P0, S10 and R8) were also analyzed by XRD at RT, taking the above-mentioned coherence of DSC data into account. In Fig. 7(a), the X-ray diffractogram denotes a ~100% volumetric fraction of the austenitic phase with cubic B2 structure, as per main characteristic peaks (110), (200) and (211), besides some tiny evidence of metastable $Ti_2Ni$ precipitates (or $Ti_4Ni_2O$ – just close diffraction pattern) mainly for Sample P0. This residual $Ti_2Ni$ (or $Ti_4Ni_2O$) is also consistent with the SEM/EDS findings, as for Sample S5 in Fig. 4(b). Although these precipitates could not be eliminated in the process because of oxygen stabilization, they became XRD-undetectable for Samples S10 and R8, likely due to reduction in their sizes [13]. In Fig. 7(b), samples crystallites sizes were estimated by using FWHM (Full Width at Half Maximum) in the Scherrer Equation. In principle, Sample S10 had the smallest crystallites as a function of ~0.8° broader FWHM, but its most intense $(110)_{B2}$ peak could also indicate the presence of sharp texture, enabling a significant difference in crystallographic orientation, as in [18–20]. In short, based on crystallites size, Sample R8 (FWHM ~0.13°) seems more structurally similar to Sample P0 (FWHM ~0.15°) in relation to Sample S10, as well as in terms of hardness trends.

Lastly, the subject XRD analysis corroborates that this Ni-rich Ti–Ni alloy remained fully austenitic (with no induced B19′ martensite, eventually it could appear as in [20]) at RT; while the DSC results revealed this original phase stability at RT, and its crystallographic reversibility (from austenite to martensite, and vice versa) was practically settled down in negative temperatures.

## 4. Conclusions

Based on the characteristics of the material, methodology and results presented:

- The secondary processing of a nickel-rich Ti–Ni shape memory alloy was analytically driven, as swaged and rolled bars, comparing them in parallel and step-by-step, despite some minor process inaccuracies (as manual feeding variables).
- For technical substantiation from a product point of view: deformation bands and grain morphology were featured throughout an essential austenitic phase at RT; the hardness trends were correlated in detail, with a similar increase at the work hardening level, from the center to the surface area, after each AR stage due to redundant work; $Ti_2Ni$ (or $Ti_4Ni_2O$) precipitates and oxidation were also confirmed as a consequence of the thermomechanical processing at the hot-condition; and the reversible MT at negative temperatures was consistent with the literature data.
- On a comparative basis, bars have been formed preferably into a duo-channel roller (unlike rotary swage with 2D dies) and by using interpass heating in a conventional furnace (better than by an inductive one), in accordance with the resulting microstructure and properties of the material for potential applications.

## Declaration of Competing Interest

The authors declare that they have no known competing financial interests or personal relationships that could have appeared to influence the work reported in this paper.

## Acknowledgments

To CAPES (grant 88887.511327/2020-00) and CNPq (grant 307654/2018-4), for the current financial support. To IPEN and ITA, for the staff and research facilities. To Villares Metals (Clayton Paspardelli) and Multialloy (Michel Bex in memoriam), for the collaboration in the production and initial processing of ingots. And, to FAPESP and FINEP, for the precursor/aligned support.

## REFERENCES

[1] Otsuka K, Ren X. Physical metallurgy of Ti-Ni based shape memory alloys. Prog Mater Sci 2005;50:511–678. https://doi.org/10.1016/j.pmatsci.2004.10.001.
[2] Porter DA, Easterling KE, Sherif MY. Phase transformations in metals and alloys. 4th ed. CRC; 2021. https://doi.org/10.1201/9781003011804.
[3] Elahinia MH. Shape memory alloy actuators: design, fabrication, and experimental evaluation. 1st ed. John Wiley & Sons; 2016.
[4] Otubo J, Rigo OD, Neto CM, Mei PR. The effects of vacuum induction melting and electron beam melting techniques on the purity of NiTi shape memory alloys. Mater Sci Eng, A 2006;438:679–82. https://doi.org/10.1016/j.msea.2006.02.171.
[5] Antunes AS, Tosetti JPV, Otubo J. High shape recovery Ni-Ti SMA wire produced from electron beam melted ingot. J Alloys Compd 2012;577:265–7. https://doi.org/10.1016/j.jallcom.2012.03.043.
[6] Kabayama LK, Rigo OD, Otubo J. Influence of thermomechanical processing on the martensitic transformation temperatures of NiTi SMA wire. Mater Sci Forum 2010;643:43–8. https://doi.org/10.4028/www.scientific.net/MSF.643.43.

[7] Antunes AS. Influence of phase transformation, drawing angle and reduction area upon SME characteristics in NiTi wires [PhD thesis]. SJC, SP: ITA; 2015.
[8] Santos LA. Shape memory effect and superelasticity of Ti-50,9Ni alloy improved by ageing under stress [PhD thesis]. SJC, SP: ITA; 2018.
[9] Verlinden B, Driver J, Samajdar I, Doherty RD. Thermo-mechanical processing of metallic materials. 1st ed. UK: Elsevier; 2007.
[10] Wright RN. Wire technology: process engineering and metallurgyvol. 18. UK: Elsevier; 2011. p. 272–6.
[11] Jiang S, Zhang Y, Zhao Y. Dynamic recovery and dynamic recrystallization of NiTi shape memory alloy under hot compression deformation. Trans Nonferrous Met Soc 2013;23:140–7. https://doi.org/10.1016/S1003-6326(13)62440-1.
[12] Xu CH, Ma XQ, Shi SQ, Woo CH. Oxidation behavior of TiNi shape memory alloy at 450–750 °C. Mater Sci Eng, A 2004;371:45–50. https://doi.org/10.1016/S0921-5093(03)00287-9.
[13] Neiman AA, Semin VO, Meisner LL, Ostapenko MG. Structural decomposition and phase changes in TiNi surface layer modified by low-energy high-current pulsed electron beam. J Alloys Compd 2019;803:721–9. https://doi.org/10.1016/j.jallcom.2019.06.322.
[14] Gall K, Tyber J, Wilkesanders G, Robertson SW, Ritchie RO, Maier HJ. Effect of microstructure on the fatigue of hot-rolled and cold-drawn NiTi shape memory alloys. Mater Sci Eng, A 2008;486:389–403. https://doi.org/10.1016/j.msea.2007.11.033.
[15] Otubo J, Rigo OD, Coelho AA, Neto CM, Mei PR. The influence of carbon and oxygen content on the martensitic transformation temperatures and enthalpies of NiTi shape memory alloy. Mater Sci Eng, A 2008;481:639–42. https://doi.org/10.1016/j.msea.2007.02.137.
[16] Shahmir H, Nili-Ahmadabadi M, Huang Y, Langdon TG. Evolution of microstructure and hardness in NiTi shape memory alloys processed by high-pressure torsion. J Mater Sci 2014;49:2998–3009. https://doi.org/10.1007/s10853-013-7985-2.
[17] Frenzel J, George EP, Dlouhy A, Somsen C, Wagner MF-X, Eggeler G. Influence of Ni on martensitic phase transformations in NiTi shape memory alloys. Acta Mater 2010;58:3444–58. https://doi.org/10.1016/j.actamat.2010.02.019.
[18] Churakova A, Gunderov D. Microstructural and mechanical stability of a Ti-50.8at.%Ni shape memory alloy achieved by thermal cycling with a large number of cycles. Metals 2020;10(227). https://doi.org/10.3390/met10020227.
[19] Lopez HF, Salinas A, Calderón H. Plastic straining effects on the microstructure of a Ti-rich NiTi shape memory alloy. Metall Mater Trans A 2001;32:717–29. https://doi.org/10.1007/s11661-001-1007-8.
[20] Prokoshkin SD, Korotitskiy AV, Brailovski V, Inaekyan E, Dubinskiy SM. Crystal lattice of martensite and the reverse of recoverable strain of thermally and thermomechanically treated Ti-Ni shape memory alloys. Phys Met Metallogr 2011;112:170–87. https://doi.org/10.1134/S0031918X11020244.